

An integrated antireflection design using nanotexture and high-refractive-index glass for organic photovoltaics

Shigeru Kubota, Yoshiki Harada, Takenari Sudo, Kensaku Kanomata,
Bashir Ahmmad, Jun Mizuno, Fumihiko Hirose

© American Coatings Association 2017

Abstract We propose a new antireflection (AR) design for organic photovoltaics (OPVs) to achieve broadband and omnidirectional enhancement of photocurrent. In the proposed design, a hybrid AR structure, which combines moth eye texturing and two-layer interference coating, is integrated with a glass substrate having a high refractive index (n). Using the optical simulation for OPV cells, we compare the performance of various AR configurations upon changing the refractive index of the glass substrate. We show that the short-circuit current density (J_{SC}) is decreased by using the high- n glass substrate without AR coating, whereas J_{SC} is significantly increased by applying the high- n glass substrate with the hybrid AR structure, suggesting an importance of the integrated design. In addition, we demonstrate that the proposed AR configuration is quite effective to attain broad angle performance and is robust against the variations in geometric features of moth eye texture. Finally, the spectral dependence of photocurrent generation is experimentally measured for the verification of the effectiveness of the integrated AR design. These results provide a practical and efficient AR technique that can further expand the potential of OPVs as energy supply devices.

Keywords Organic solar cell, Antireflection, Moth eye, Optical simulation

S. Kubota (✉), Y. Harada, K. Kanomata
B. Ahmmad, F. Hirose
Graduate School of Science and Engineering, Yamagata
University, 4-3-16 Jonan, Yonezawa, Yamagata 992-8510,
Japan
e-mail: kubota@yz.yamagata-u.ac.jp

T. Sudo, J. Mizuno
Research Organization for Nano and Life Innovation,
Waseda University, 513 Wasedaturumaki-cho,
Shinjyuku-ku, Tokyo 162-0041, Japan

Introduction

Many recent studies suggest that organic photovoltaics (OPVs) are promising as a key for energy supply because they have a high potential for low-cost, large-area, and flexible power generation devices in the near future.^{1–4} OPVs are also expected to perform as excellent indoor solar cells, due to their high fill factor under low light intensities and the absorption band matching the indoor light spectrum.^{5–8} The power conversion efficiency of bulk heterojunction OPVs has been significantly improved in the last decade, although further improvements will be required for large-scale commercialization.⁹ A main limitation for enhancing the performance of OPVs is the difficulty in achieving a trade-off balance between the light absorption and exciton harvesting efficiency.^{10,11} Due to a small exciton diffusion length of organic polymers, the thickness of active layer (typically ~ 100 nm thick) should be much smaller than that required for fully absorbing incident light. Therefore, it is highly desirable to develop an efficient antireflection structure (ARS) for trapping light in such thin active layer.

In order to realize broadband and wide-angle antireflection (AR) coatings, recent studies are focusing on the moth eye texture, a nanostructure inspired by the corneal surface of the eyes of certain species of moths.^{12–20} In the moth eye coating, the device surface is covered with two-dimensional cone array with a period and height of a few hundred nanometers. This textured surface functions to produce a gradual change in the refractive index (n) from that of the incident medium to the device, suppressing reflection across wide spectral regions.¹⁸ Such gradient index profile also plays a critical role in weakening reflection at large incident angles by producing smooth optical path of incident light.²⁰

When the moth eye coating is applied to OPVs, it is additionally important that the textured material

should have compatibility with the advantages of OPVs, such as low-cost and large-area manufacturing. From this viewpoint, organic polymers are highly beneficial, because the large-area textured surfaces can be fabricated cost-effectively by nanoimprint lithography with polymeric resists.^{21–25} However, since the organic polymers are low- n materials with a narrow adjustable range of refractive index (around 1.5),²⁶ the use of polymers for the front surface of OPVs necessarily causes the optical mismatch between the low- n textured surface and the high- n materials in OPV itself such as indium-doped tin oxide (ITO). The effects of such optical mismatch should be suppressed by adequately designing the refractive index profile of the whole OPV device.

Therefore, in this study, we propose a new optical design for an OPV device to attain the improved overall refractive index profile in the presence of moth eye surfaces made by nanoimprint lithography. In this device design, the hybrid ARS proposed by our recent study,¹² which combines moth eye and interference (IF) multilayer, is integrated with a high- n glass substrate. We numerically analyze the optical properties of OPVs with various AR configurations using the characteristic matrix-based method.²⁷ We show that the use of the high- n glass substrate without ARS is not effective to improve the performance but that the concurrent use of the high- n glass substrate and the hybrid ARS results in broadband and wide-angle performance enhancement, suggesting a significance of the integrated design. We also demonstrate that the proposed AR configuration has high performance even when there is a variation in the residual layer thickness and a spatial clearance between the moth eye cones, which arises in the nanoimprint process.²⁸ Finally, we experimentally measure the spectrum of external quantum efficiency (EQE) to verify the effectiveness of the proposed AR design. These results offer a practical optical design method to improve light trapping function of OPV devices.

Experimental

Optical modeling

Numerical simulations were conducted to study the dependence of the efficiency of OPVs on the AR configuration. Figure 1a shows the structure of an OPV cell without ARS, which serves as a reference for evaluating performance. The active layer is a 100-nm film of poly(3-hexylthiophene) (P3HT) and [6,6]-phenyl-C₆₁-butyric acid methyl ester (PCBM) blend (1:1 by weight), and the hole transporting layer is a 7-nm MoO₃ film. These materials are sandwiched by a transparent front electrode of a 150-nm ITO layer and a back electrode of 100-nm Al layer. The OPV cell is attached to the glass substrate with the thickness of 0.7 mm.

Figure 1b illustrates an OPV cell with the hybrid ARS, which consists of moth eye array and two-layer IF film.¹² The IF film consists of MgF₂ and Al₂O₃ layers, both of which are frequently used for AR coatings, e.g., in reference 29. Throughout this study, the layer order and thicknesses of the IF layers are selected to maximize short-circuit current density (J_{SC}) under the AM1.5 solar spectrum³⁰ by numerical optimization.³¹ In the moth eye structure, the cones with the same size are hexagonally arranged. The base circles of two adjacent cones are assumed to touch each other in all the simulations except those for Fig. 6a, where the effects of the clearance between adjacent cones are examined. The geometric pattern of moth eye is determined by the period L of cone array as well as the diameter D and height H of each cone. Unless otherwise stated, we used the values of $L = D = 250$ nm and $H = 500$ nm, which are within a typical range of parameter values used for moth eye texture.^{32–35} We assumed that the moth eye surface is fabricated by the nanoimprint lithography with polymeric resists because the nanoimprint process is quite appropriate for low-cost production of large-area nanostructures, as mentioned above.^{21–25} Accordingly, the refractive index of the moth eye structure is set to be 1.5, which is a typical value for organic polymers.²⁶ In order to predict how the AR function is affected by the existence of residual layer, which remains in the nanoimprint resist,^{28,32,36} a thin film representing the residual layer was added adjacent to the moth eye structure (Fig. 1b).

The AR design proposed in this study is shown in Fig. 1c. In the proposed design, the hybrid ARS is integrated with the glass substrate having a refractive index of around 1.5–2, which is higher than that of a normal glass substrate (around 1.5) (Fig. 2a). The use of the higher refractive index value for the glass substrate is aimed at decreasing the reflection at the back side of the substrate though decreasing the optical mismatch between the glass substrate and the materials in the OPV cell (see Results and discussion). In addition, we analyzed the optical property of the OPV device that has only the two-layer IF coating or the moth eye coating for comparison to the device with the proposed AR configuration (Fig. 1c).

We used two types of optical parameters for the glass substrate in the characteristic matrix-based analysis (see below): one is the parameter obtained by the measurement of spectroscopic ellipsometry (Fig. 2a). The other is the simplified parameter with a constant refractive index of n_G and zero extinction coefficient for all wavelengths. The simplified parameter is used in Figs. 3, 4, 5, 6 and 9 to analyze the effects of changing the refractive index profile of the device. The measurement of optical data for the materials in the OPV cell was performed with a JASCO M-220 spectroscopic ellipsometer. To obtain the optical properties of thin-film materials, both the parameters in the optical model (e.g., the Lorentz-Drude model^{37,38}) and the

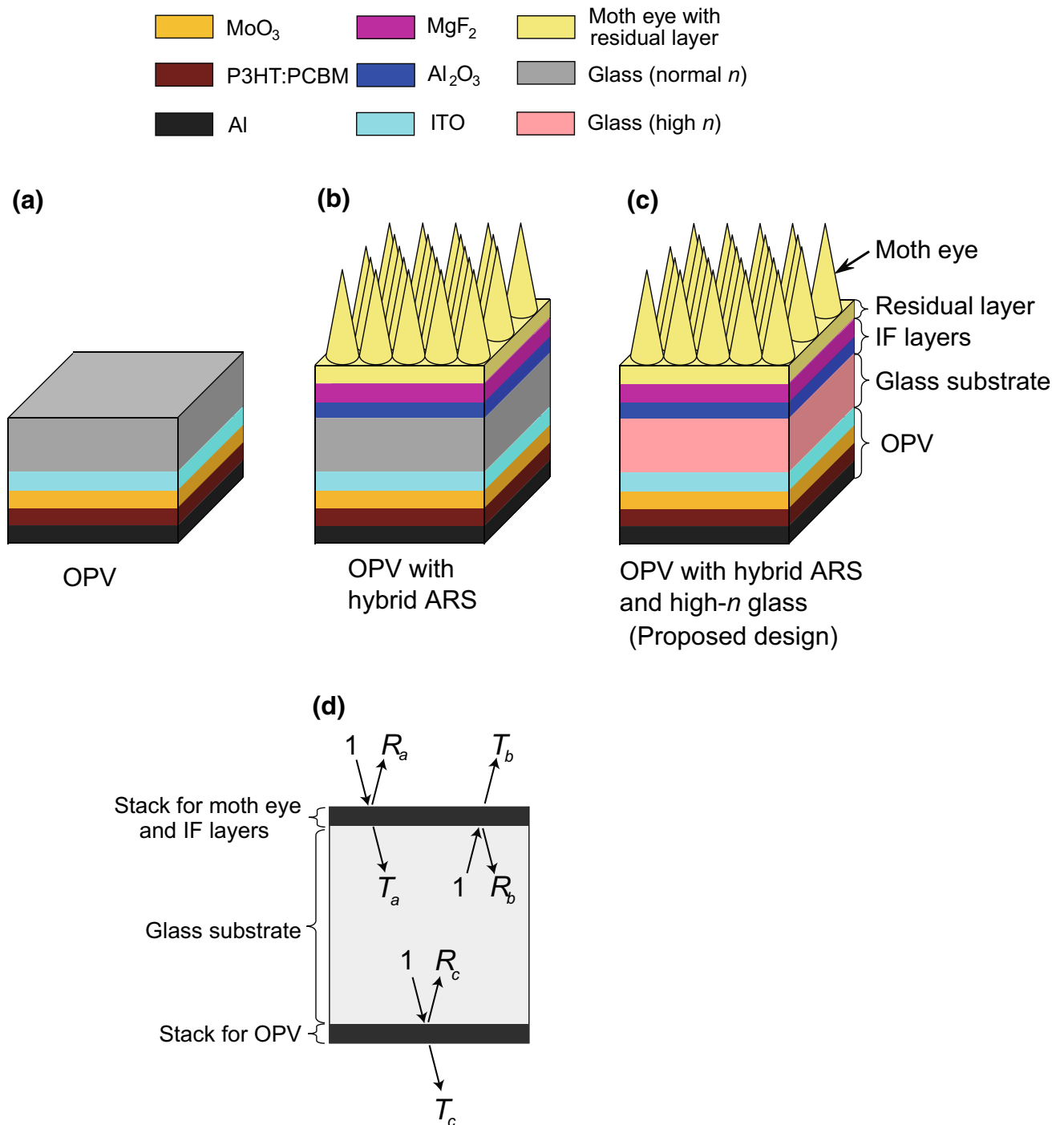
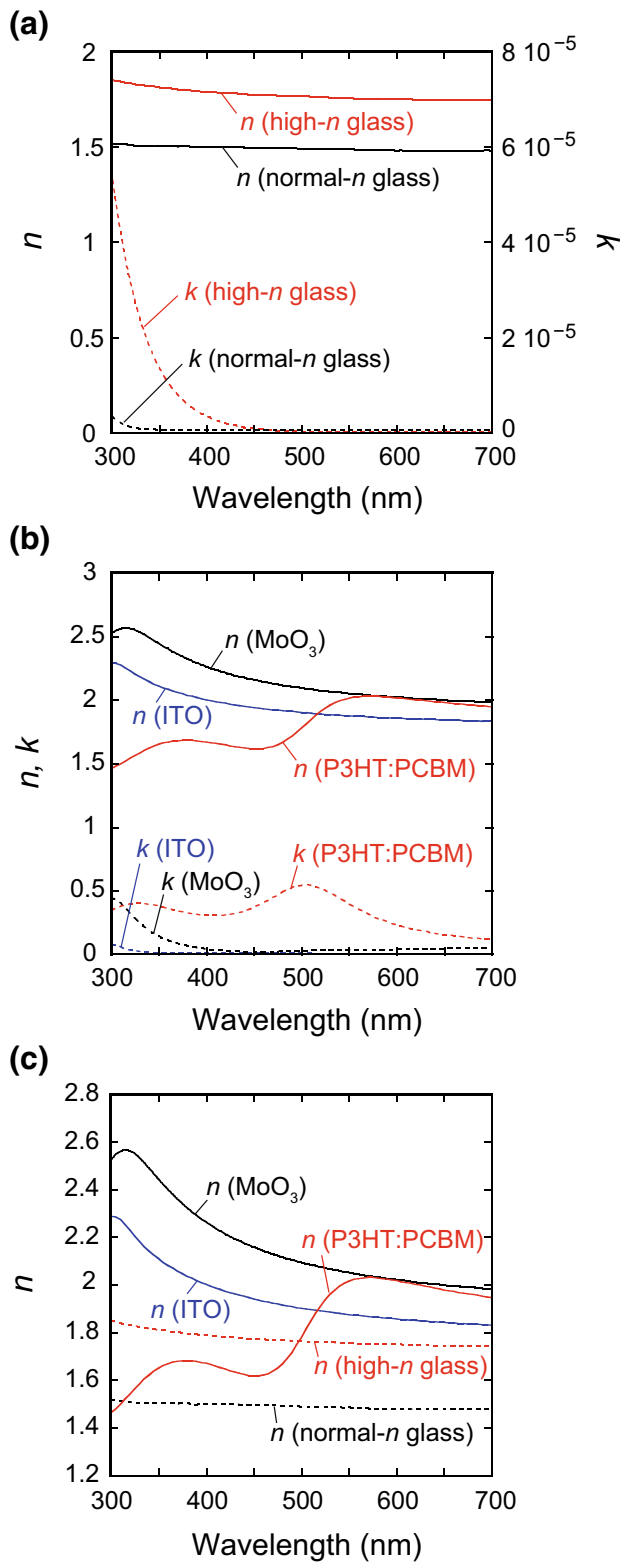


Fig. 1: (a–c) Structures of a reference OPV cell (a), an OPV cell with the hybrid ARS (b), and an OPV cell with the hybrid ARS and the high-*n* glass substrate (c). The structure in (c) shows the AR design proposed in the current study. (d) In the characteristic matrix-based analysis, the device with the hybrid ARS is considered to be an assembly of a thick glass substrate and two multilayer stacks (i.e., a stack representing the moth eye and IF layers and another stack representing the OPV cell)



◀Fig. 2: The optical data of the materials in OPVs obtained by the measurements of spectroscopic ellipsometry. (a) Comparison between the optical parameters for a typically used glass substrate (black) and the high-*n* glass substrate used in our experiment (red). (b) The optical data of MoO₃ (black), P3HT:PCBM (red), and ITO (blue). In (a) and (b), the solid and dashed lines represent the values of refractive index (*n*) and extinction coefficient (*k*), respectively, as a function of wavelength. (c) Summary of the refractive index values of all the materials in (a) and (b) (Color figure online)

value of film thickness were fitted together to the ellipsometry data for the wavelength range between 300 and 700 nm. The examples of the wavelength-dependent optical parameters are shown in Fig. 2.

Effective medium approximation

The optical property of moth eye structure was modeled by applying the effective medium theory.³⁹ This theory is widely used to describe the optical characteristics of nanotextures when the period of textured pattern is sufficiently small compared to the wavelength of incident light.¹⁹ To apply the effective medium theory, each cone in the moth eye array was divided by planes, which are parallel to the base, into many thin layers with 2 nm thickness. The effective permittivity ϵ for each thin layer was decided from the following equation³⁹:

$$f_a \frac{\epsilon_a - \epsilon}{\epsilon_a + 2\epsilon} + (1 - f_a) \frac{\epsilon_0 - \epsilon}{\epsilon_0 + 2\epsilon} = 0, \quad (1)$$

where f_a is the volume fraction of moth eye structure in the thin layer, ϵ_a is the permittivity of the material used for moth eye, and ϵ_0 is the permittivity of free space.

To estimate the accuracy of the effective medium approximation in our model, the finite-difference time-domain (FDTD) simulation⁴⁰ was performed to calculate J_{SC} of the OPV cell with the moth eye with various periods (L) (Fig. 8a; see Appendix 1 for the detail of FDTD simulation). We estimated the relative change in J_{SC} compared to the case with $L = 32$ nm, which is much smaller than the wavelength of sunlight (> 300 nm) and is therefore within the length scale where the effective medium approximation can be reasonably applied. The result showed that for the L values used in this study ($L < 300$ nm), the relative change in J_{SC} is less than 0.2% (Fig. 8b). Given that this value is much smaller than the increase in J_{SC} by applying moth eye texturing (>3.5%; Fig. 3b), the effective medium approximation can be considered accurate enough for the current analysis.

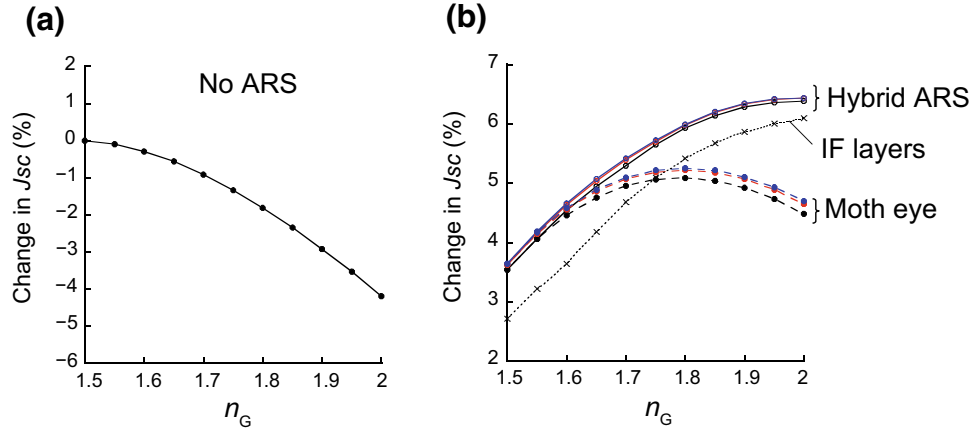


Fig. 3: Changes in J_{SC} as a function of the refractive index of the glass substrate (n_G). (a) The case in the absence of antireflection. (b) The cases of applying the hybrid ARS (solid lines), IF layers (dotted line), or moth eye coating (dashed lines). The color of the solid and dashed lines represents the height H of cone array used in the hybrid ARS and moth eye structure: $H = 250$ (black), 500 (red), or 1000 nm (blue). In (a) and (b), the reference value of J_{SC} from which the changes are calculated is that obtained by the OPV cell which has a glass substrate with a normal refractive index ($n_G = 1.5$) and does not have ARS (Color figure online)

Characteristic matrix-based analysis

To evaluate the performance of OPVs, we calculated the value of J_{SC} by using the characteristic matrix-based method²⁷ for all the optical simulations except for that for Fig. 8. By applying the effective medium theory, the moth eye structure is described as a multilayer stack with a graded refractive index profile. Therefore, the OPV cell with the hybrid ARS (Fig. 1c) can be considered to consist of two thin-film stacks (i.e., the stack for the moth eye and IF layers and the stack for the OPV cell) and a much thicker glass substrate, as shown in Fig. 1d. In each of the two stacks, light is added coherently according to the characteristic matrix-based formalism, whereas in the thick substrate, the addition of irradiances (not electric field amplitudes) is considered due to a loss of coherence.^{13,31,41,42}

By using the characteristic matrix method, the reflectance R and transmittance T , for a multilayer thin-film stack (with q layers), are obtained as follows^{13,27,31}:

$$R = \left(\frac{\eta_i B - C}{\eta_i B + C} \right) \left(\frac{\eta_i B - C}{\eta_i B + C} \right)^* \quad (2)$$

and

$$T = \frac{\text{Re}(\eta_e)}{\text{Re}(\eta_i)} \left(\frac{2\eta_i}{\eta_i B + C} \right) \left(\frac{2\eta_i}{\eta_i B + C} \right)^* \quad (3)$$

Here, η_i and η_e represent the tilted optical admittances (see below) for the incident and emergent media, respectively, and B and C are given by

$$\begin{bmatrix} B \\ C \end{bmatrix} = M_1 M_2 \dots M_q \begin{bmatrix} 1 \\ \eta_e \end{bmatrix} \quad (4)$$

The characteristic matrix M_r for the r th layer ($r = 1, \dots, q$) is described as

$$M_r = \begin{bmatrix} \cos \delta_r & (i \sin \delta_r) / \eta_r \\ i \eta_r \sin \delta_r & \cos \delta_r \end{bmatrix}, \quad (5)$$

with the phase difference δ_r between the top and bottom of the r th layer. The tilted optical admittances η_i , η_e , and η_r for the s - and p -polarized light are given as follows:

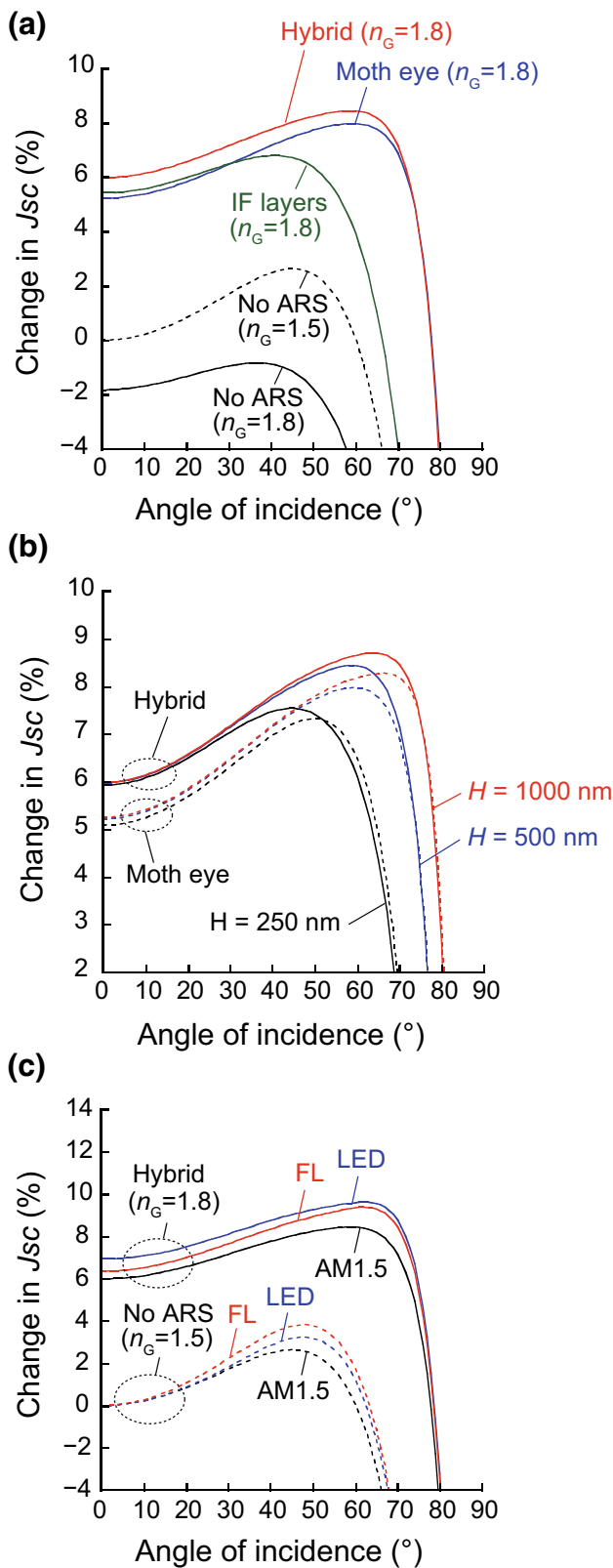
$$\eta_X = \begin{cases} y_f N_X \cos \theta_X & (\text{for } s\text{-polarization}) \\ y_f N_X / \cos \theta_X & (\text{for } p\text{-polarization}) \end{cases}, \quad (6)$$

with $X = i, e, \text{ or } r$. Here, y_f is the optical admittance of free space, and N_X is the complex refractive index for the corresponding medium or layer. θ_i is the incident angle, and θ_e and θ_r are the complex angles determined by the Snell's law $N_i \sin \theta_i = N_r \sin \theta_r = N_e \sin \theta_e$.

By considering the multiple reflection at the interfaces between the glass substrate and the two stacks (Fig. 1d), the overall reflectance R_t at the front surface and the absorbance A_0 in the glass substrate are, respectively, described as

$$R_t = R_a + \frac{T_a T_p^2 R_c T_b}{1 - T_p^2 R_b R_c} \quad (7)$$

and



◀Fig. 4: Dependence of J_{SC} on the angle of incidence. (a) Black lines: the cases without ARS when the refractive index of glass substrate (n_G) is set as 1.5 (dashed) or 1.8 (solid). Colored lines: the cases of applying the hybrid ARS (red), IF layers (green), or moth eye (blue) for $n_G = 1.8$. The height of cone array used for the hybrid ARS and moth eye structure is $H = 500$ nm. (b) The solid and dashed lines represent the cases of applying the hybrid ARS and moth eye coating, respectively, for $n_G = 1.8$ with $H = 250$ (black), 500 (blue), or 1000 nm (red). (c) The angle-dependent property under the light sources of AM1.5 (black), LED (blue), and fluorescent lamp (red). Solid lines: the cases of applying the hybrid ARS for $n_G = 1.8$. Dashed lines: the cases without ARS for $n_G = 1.5$. In (a)–(c), the y-coordinate is the relative change in J_{SC} from the reference value, which is defined as the value of J_{SC} obtained by the OPV cell that has a glass substrate with $n_G = 1.5$ and does not have ARS. In (c), the reference value of J_{SC} is set separately for each light source condition (Color figure online)

$$A_0 = \frac{T_a(1 - T_p)(1 + R_c T_p)}{1 - T_p^2 R_c R_b} \quad (8)$$

Here, R_a , R_b , R_c , T_a , and T_b are the reflectance and transmittance for each stack, which are defined as shown in Fig. 1d, and T_p is the internal transmittance of the glass substrate. If we define I_S to be the irradiance of the light entering the stack for the OPV cell, I_S can be obtained by the energy conservation law as follows:

$$I_S = 1 - R_t - A_0. \quad (9)$$

If the active layer is assumed to be the p th layer in the multilayer stack for the OPV cell, the absorbance in the active layer, A_p , can be described as

$$A_p = I_S(\psi_{p-1} - \psi_p), \quad (10)$$

$$\psi_r = \frac{\text{Re}(B_r C_r^*)}{\text{Re}(B C^*)} \quad (\text{for all } r) \quad (11)$$

$$\begin{bmatrix} B_r \\ C_r \end{bmatrix} = M_{r+1} M_{r+2} \dots M_q \begin{bmatrix} 1 \\ \eta_e \end{bmatrix}. \quad (12)$$

Here, ψ_r is the potential transmittance for the sub-assembly including the thin films from the front side to the r th layer in the multilayer stack for the OPV cell.²⁷

We represent the absorbance in the active layer at wavelength λ as $A_p(\lambda)$. Then, the number of photons $N_p(\lambda)$ absorbed in the active layer, corresponding to λ , is expressed as

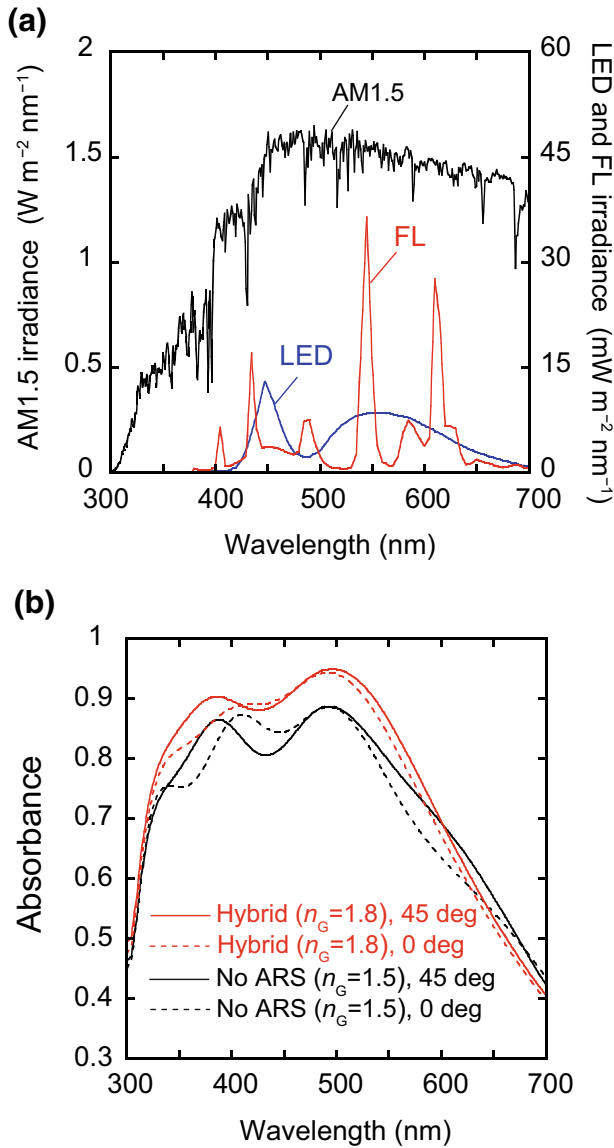


Fig. 5: (a) The irradiance spectra for the sunlight (AM1.5) (black), LED (blue), and fluorescent lamp (FL) (red).^{5,30,44} (b) The spectra of the absorbance in the active layer for normal incidence (dashed lines) and oblique incidence (45 deg, solid lines). Black lines: the cases where the ARS is not applied and the normal-*n* glass substrate of *n_G* = 1.5 is used (i.e., the cases of the reference OPV cell). Red lines: the cases where the hybrid ARS is applied with the high-*n* glass substrate of *n_G* = 1.8 (i.e., the cases with the proposed AR design) (Color figure online)

$$N_p(\lambda) = A_p(\lambda)F(\lambda) \frac{\lambda}{hc}, \quad (13)$$

where $F(\lambda)$ is the irradiance spectrum of incident light, which is assumed to be the AM1.5 solar spectrum³⁰ unless otherwise stated. h is Planck's constant, and c is the light speed in free space. With the elementary charge q_e , the number of photons can be converted into the photocurrent as follows:

$$J_{SC} = \int_0^{\lambda_g} q_e N_p(\lambda) F_{NR}(\lambda) d\lambda, \quad (14)$$

where λ_g is the wavelength corresponding to the bandgap energy of P3HT (653 nm). $F_{NR}(\lambda)$ represents the nonrecombination factor, which is simply assumed to be $F_{NR}(\lambda) = 1$ for all values of λ .⁴³

Incident light condition

Since OPVs are suggested to be promising for indoor application,^{5–8} we investigated the AR performance of the proposed device design using the light sources of not only sunlight (AM1.5 standard³⁰) but also light emitting diode (LED) and fluorescent lamp. The irradiance spectra of LED and fluorescent lamp were taken from the data for cool LED⁵ and F11,⁴⁴ respectively, as the representative examples for indoor light sources.⁵ The irradiance spectra for the indoor light sources are scaled to 500 lx, which is a value recommended for general offices.⁵ For the incident angle condition, the normal incidence was assumed for all the figures except for Figs. 4 and 5, where the wide-angle property was examined. In the case of oblique incidence, to treat the input as the unpolarized light, the averaging of the optical response obtained by the *s*- and *p*-polarized light waves was performed.⁴⁵

Device fabrication and testing

The OPV cell was experimentally constructed with the same structure as that of the optical model (i.e., ITO/MoO₃/P3HT:PCBM/Al). A high-*n* glass substrate (OMG, N75; 20 mm × 20 mm × 0.7 mm) with $n_D = 1.75$ (Fig. 2a, red lines), coated by 150-nm-thick ITO (9 Ω/square), was cleaned in an ultrasonic bath with acetone, isopropanol, and deionized water and then cleaned by UV/ozone. To form the two-layer IF film on the side of the glass substrate without ITO coating, a 73-nm Al₂O₃ layer was sputtered and thereafter a 170-nm MgF₂ layer was evaporated. The thicknesses of the MgF₂ and Al₂O₃ layers were determined to maximize J_{SC} through numerical optimization.³¹ After the 7-nm MoO₃ layer was evaporated on the ITO film, the 100-nm P3HT:PCBM (1:1 by weight) photoactive layer was spin coated on the surface of the MoO₃ layer. Lastly, as a back electrode, the 100-nm Al layer was evaporated on the top of the polymer film, and the device was annealed at 130°C for 15 min under a nitrogen atmosphere.

For fabricating moth eye texture, a glass substrate having a typical value of refractive index ($n_D = 1.5$; 20 mm × 20 mm × 0.7 mm) was cleaned with organic solvents and UV/ozone, similar to the above-mentioned method. A UV curable resin (Toyo Gosei, PAK01) was spin coated onto the substrate with a thickness of 700 nm, which was followed by annealing

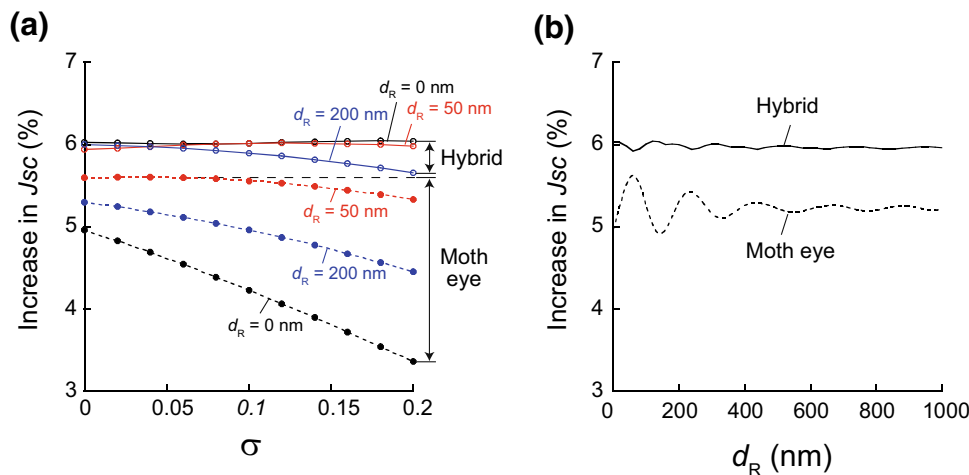


Fig. 6: Effects of the variations in the geometric features of moth eye texture produced by nanoimprint lithography. (a) The increase in J_{SC} by applying the hybrid ARS (solid lines) or moth eye coating (dashed lines) is plotted as a function of σ , for the residual layer thickness $d_R = 0$ (black), 50 (red), or 200 nm (blue). The parameter σ is a nondimensional quantity between 0 and 1 to represent the relative size of the clearance between adjacent cones in moth eye array. (b) The increase in J_{SC} by the hybrid ARS (solid line) or moth eye coating (dashed line) as a function of d_R ($\sigma = 0$). In (a) and (b), the high- n glass substrate with $n_G = 1.8$ is used (Color figure online)

at 80°C for 2 min. The moth eye texture with 260 nm period and 320 nm height (pattern size: 10 mm × 10 mm) was replicated in the resin by the nanoimprint lithography, by using the mold produced by Toppan Printing.

To construct the OPV device with the proposed AR design, we combined the two glass substrates that were processed as described above (i.e., the high- n glass substrate with the OPV and IF layers and the normal- n glass substrate with moth eye). Both the glass substrates were connected by putting between them the contact liquid whose refractive index was adjusted to match that of the normal- n glass substrate ($n_D = 1.5$). This fabrication method was adopted for the sake of convenience in comparing the performance of the devices with different AR conditions. The device configuration can be summarized as moth eye/normal- n glass/contact liquid/IF layers/high- n glass/OPV. Importantly, the nanoimprint resin used for fabricating moth eye (Toyo Gosei, PAK01) is selected such that its refractive index is very close to that of the normal- n glass and contact liquid ($n_D = 1.5$), meaning that the materials of the moth eye, normal- n glass, and contact liquid have nearly the same refractive index values. Therefore, the fabricated device is approximately optically equivalent to the configuration of moth eye/IF layers/high- n glass/OPV. This configuration is basically the same as that of the proposed AR design shown in Fig. 1c, where the residual layer corresponds to the normal- n glass substrate and contact liquid. To evaluate the photocurrent generation property, the spectral change in EQE was measured in air at room temperature, using a Bunko-keiki CEP-2000TF system. The EQE spectrum ($EQE(\lambda)$) was numerically converted to the level of J_{SC} for the light sources of

sunlight, LED, and fluorescent lamp by using the corresponding irradiance spectrum data ($F(\lambda)$) as follows^{5,46}:

$$J_{SC} = \int q_e EQE(\lambda) F(\lambda) \frac{\lambda}{hc} d\lambda.$$

Results and discussion

Effectiveness of the AR design with hybrid ARS and high- n glass substrate

We numerically analyzed the optical property of OPVs to investigate the effectiveness of the proposed AR design (Fig. 1c). We first made a comparison of the optical parameters for the materials used in an OPV cell (Fig. 2). As shown in Fig. 2c, a typical refractive index of glass substrate (around 1.5) (black dashed line) is lower than that of ITO, MoO₃, and P3HT:PCBM (colored solid lines) for almost all wavelengths. This predicts that increasing the refractive index of glass substrate can decrease the mismatch in optical admittance between the glass substrate and the thin-film assembly of the OPV cell to weaken the reflection at the interface between them.²⁷

Therefore, by using the characteristic matrix-based analysis, we analyzed the effects of changing the refractive index of glass substrate (n_G) on the performance of OPVs with various AR configurations (Fig. 3). As shown in Fig. 3a, larger n_G decreased J_{SC} in the absence of antireflection. On the other hand, when the hybrid ARS or the two-layer IF coating was

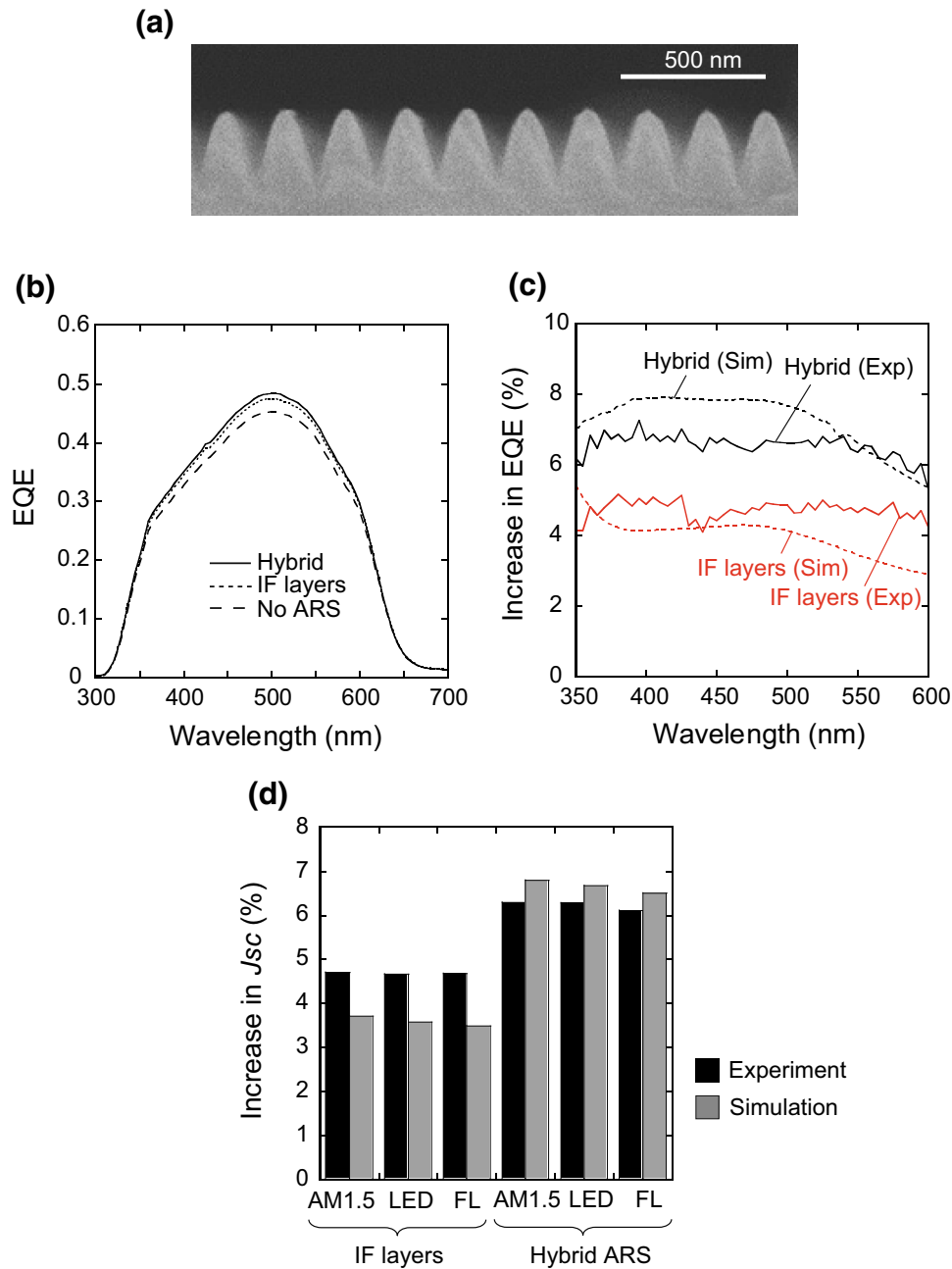


Fig. 7: The experimental results to test the effectiveness of the proposed AR design and their comparison with the simulation results. (a) SEM micrograph of the moth eye structure. The scale bar is 500 nm. (b) Experimentally measured EQE spectra. Solid and dotted lines: the cases of the OPV cell with the hybrid ARS (solid line) or the IF coating (dotted line). Dashed line: the case of the reference OPV cell without ARS. (c) The increase rate of EQE produced by applying the hybrid ARS (black) or the IF coating (red). The solid and dashed lines correspond to the experimental and simulation results, respectively. For the simulation, we used a model of moth eye structure that has the array of rounded cones with the geometric parameters taken from the SEM image. (d) The increase rate of J_{sc} by the hybrid ARS and the IF coating is estimated from the EQE spectra obtained by the experiment (black bars) and simulation (gray bars). The results obtained by the light sources of sunlight (AM1.5), LED, and fluorescent lamp (FL) are compared (Color figure online)

applied, larger n_G was found to increase J_{sc} (Fig. 3b, solid and dotted lines). Further, when the moth eye coating was applied, larger n_G increased and decreased J_{sc} in the ranges of small and large values of n_G , respectively, producing a peak value of J_{sc} at $n_G =$

~ 1.8 (Fig. 3b, dashed lines). Changing the height of moth eye array was not found to significantly alter the level of J_{sc} . Thus, we can say that the relation between n_G and J_{sc} is qualitatively changed by the types of ARS such that the function $J_{sc}(n_G)$ is monotonically

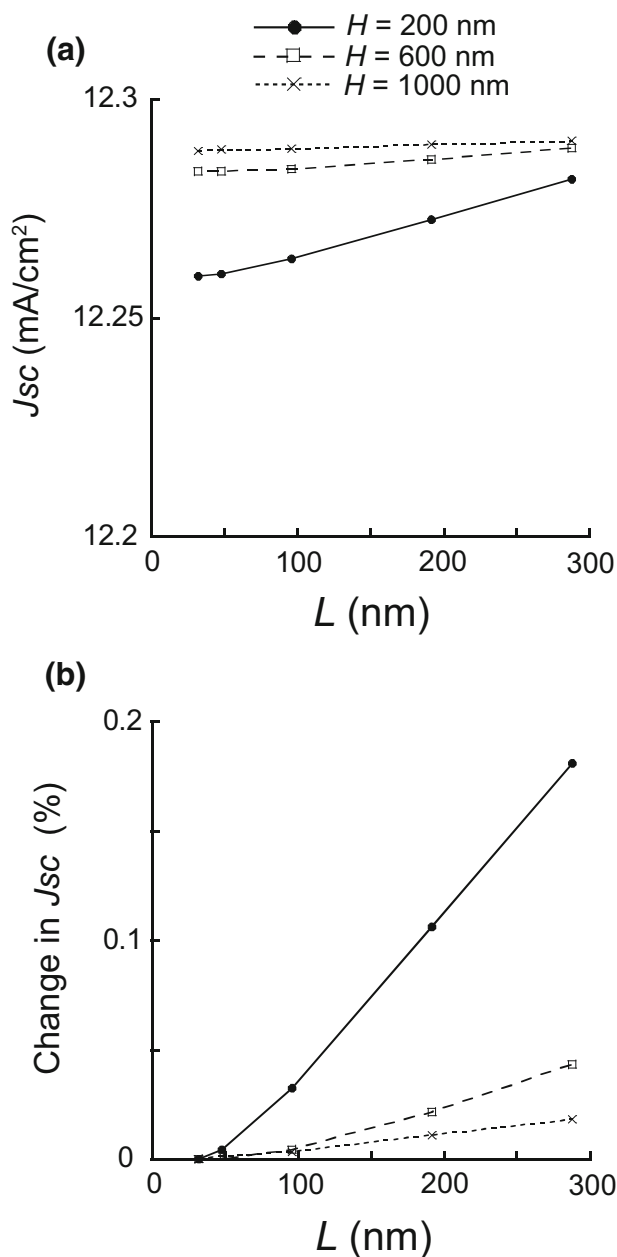


Fig. 8: Results of the FDTD analysis. (a) The change in J_{sc} as a function of the moth eye period L . (b) The relative change in J_{sc} , compared to the value obtained with $L = 32$ nm, as a function of L . In (a) and (b), the height of moth eye array is $H = 200$ (solid line), 600 (dashed line), or 1000 nm (dotted line)

decreasing without ARS, monotonically increasing with the hybrid ARS or IF coating, and has a local peak with the moth eye coating (Fig. 3). This result suggests that it is highly required to select an adequate combination of the refractive index of glass substrate and the AR configuration.

To elucidate the reason why the effect of changing n_G strongly depends on the AR configuration, we

analyzed in detail the change in the reflection at both the front and back sides of the substrate in Appendix 2. The argument in the appendix can be summarized as follows. When the refractive index of the glass substrate is increased, the reflection at the back side of the substrate is reduced by the decrease in the optical mismatch between the glass substrate and the materials in the OPV cell (Figs. 9b–9e, red lines), as expected from the optical data (Fig. 2c). However, without ARS, this effect is overcome by the increase in the reflection at the front side of the substrate, due to a greater optical mismatch between the glass and air, resulting in larger overall reflection (Fig. 9b). Importantly, for the usage of the high- n glass substrate to be effective for decreasing overall reflection, the reflection at the front side of the substrate should be sufficiently small, as compared to the reflection at the back side of the substrate. In the case of applying the hybrid ARS, due to the near absence of front-side reflection, the reduction in the back-side reflection brought by the high- n glass directly leads to a decrease in the total reflection (Fig. 9c). Since the front-side reflection can be almost fully suppressed by the hybrid ARS but not by the other AR configurations (Figs. 9b–9e, blue lines), the hybrid ARS can be considered the most useful, among the examined AR designs, to bring out the full potential of the high- n glass substrate and improve the efficiency of OPVs.

Wide-angle AR performance

We explored how the use of a high- n glass substrate affects the performance at wide incident angles for different AR configurations. Similar to the results obtained with normal incidence (Fig. 3), the increase in n_G from 1.5 to 1.8 was found to improve and worsen the wide-angle performance in the presence and absence of antireflection, respectively (Fig. 4a). However, in contrast to the cases of normal incidence, applying the hybrid ARS or moth eye (Fig. 4a, red and blue lines) was much more effective to improve the performance at large incident angles than applying the IF layers (Fig. 4a, green line). This can be explained by the results of the previous studies^{20,47} that suggest that a high AR performance at oblique angles requires a smoothness of variation in effective refractive index which can be realized in subwavelength textured surfaces. Furthermore, the performance at large incident angles ($>60^\circ$) for the devices with the hybrid ARS and with the moth eye was similarly improved by increasing the height of cone array (Fig. 4b). These results suggest that the proposed AR design possesses excellent omnidirectional performance which is intrinsic to the gradient index moth eye texture.

Recent studies suggest that OPVs are particularly promising as indoor solar cells, due to their relatively high efficiency at low light intensities^{5–8} as mentioned above. Therefore, in Fig. 4c, we compared the wide-angle property of the OPV cell with the proposed AR

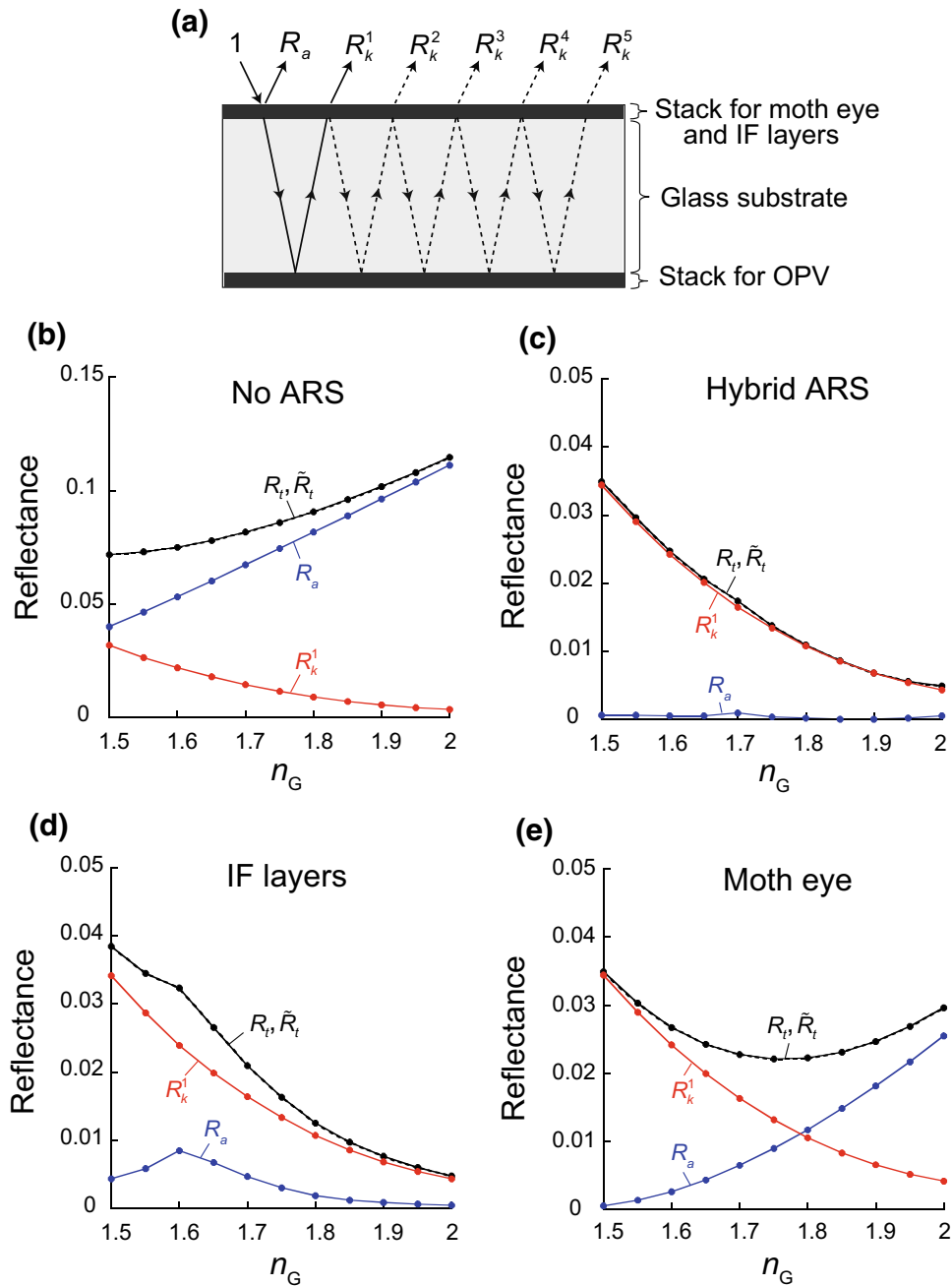


Fig. 9: The change in reflectance associated with the change in the refractive index of glass substrate (n_G) for various AR configurations ($\lambda = 500$ nm). (a) The OPV device consisting of a glass substrate and two thin-film stacks are illustrated (as in Fig. 1d) with the light waves reflected repeatedly at the front and back sides of the substrate. R_a is the irradiance of the light reflected at the front side of the substrate. R_k^n is the irradiance of the light that has been reflected n times at the back side of the substrate and returns to the incident medium. (b–e) The black dashed and solid lines show the changes in the overall reflectance R_t (equation (17)) and its approximated value \tilde{R}_t (equation (18)), respectively, as a function of n_G . (The difference between R_t and \tilde{R}_t is indistinguishable for all the cases.) The blue and red lines show the changes in R_a and R_k^1 , respectively. (b) The case of the OPV device without ARS. (c–e) The cases of the OPV device with the hybrid ARS (c), two-layer IF coating (d), or moth eye coating (e) (Color figure online)

design (solid lines) and that of the reference cell (dashed lines), under the light sources of sunlight, LED, and fluorescent lamp. The figure shows that the wide-angle AR property can be significantly improved

by the proposed design for both the outdoor and indoor light sources. This result can be understood from the fact that the light absorption is highly enhanced by the proposed AR system across a wide

Table 1: Comparison of the values of ΔJ_{SC}^G (equation (15)), J_{SC} , and the ratio $\Delta J_{SC}^G/J_{SC}$ for the three device structures of OPVs: the device without ARS and with the normal glass substrate (i.e., the reference cell), the device without ARS and with the high- n glass substrate, and the device with the hybrid ARS and the high- n glass substrate (i.e., the proposed design)

Device structure	ΔJ_{SC}^G (mA/cm ²)	J_{SC} (mA/cm ²)	$\Delta J_{SC}^G/J_{SC} \times 100$ (%)
No ARS with normal- n glass	0.16	12.66	1.27
No ARS with high- n glass	0.40	12.27	3.23
	(+145.4%)	(−3.11%)	(+153.3%)
Hybrid ARS with high- n glass	0.43	13.17	3.25
	(+165.4%)	(+4.02%)	(+155.1%)

The entries in parentheses show the relative change in each value (in percentage) compared to the value for the reference cell. The optical data used for both the normal and high- n glass are obtained by the measurements of spectroscopic ellipsometry (Fig. 2a)

Table 2: The J_{SC} value obtained from the experimentally measured EQE data for the OPV cells without ARS, with the hybrid ARS, and with the IF layers. Both the outdoor (AM1.5) and indoor (LED and fluorescent lamp) light sources are considered

AR configuration	J_{SC} (mA/cm ²)		
	AM1.5	LED	Fluorescent lamp
No ARS	5.57	2.10×10^{-2}	2.02×10^{-2}
Hybrid ARS	5.92	2.23×10^{-2}	2.14×10^{-2}
	(+6.29%)	(+6.27%)	(+6.10%)
IF layers	5.83	2.20×10^{-2}	2.11×10^{-2}
	(+4.69%)	(+4.66%)	(+4.67%)

The values in parentheses show the relative increase in J_{SC} (in percentage) as compared to the case without ARS. The values of J_{SC} under the AM1.5 spectrum are much smaller than the values estimated by the optical simulation in Table 1. This is because the nonrecombination factor $F_{NR}(\lambda)$ (equation (14)) is assumed to be 1 for all wavelengths in the simulation

wavelength range (from 320 to 630 nm; Fig. 5b), which contains the spectral region where both the outdoor and indoor lights have strong intensity (Fig. 5a).^{5,6}

Robustness against variations in geometric features of moth eye structure

When the moth eye structure is fabricated by nanoimprint lithography, as assumed in this study, it is important to evaluate how the existence of a residual layer and the spatial clearance in the moth eye array, which necessarily arise in the printing process,^{28,32,36} could degrade the performance. Therefore, we analyzed the effects of these processing-dependent factors on the performance of the OPV cell with the hybrid ARS or moth eye coating (Fig. 6). We define a measure $\sigma = (L - D)/L$, with the period L and the diameter D of each cone in the moth eye array. σ is a quantity between 0 and 1 to represent the size of the gap between adjacent cones relative to the texture period. We plotted in Fig. 6a (dashed lines) the increase in J_{SC} by the moth eye coating, as a function of σ , for the case of using the high- n glass substrate with $n_G = 1.8$. Larger σ was found to decrease J_{SC}

while the level of decrease significantly depends on the thickness d_R of the residual layer. The effect of changing d_R on J_{SC} is not monotonic, but the J_{SC} value has periodicity with respect to d_R (Fig. 6b, dashed line). This will be attributable to the interference effect of light passing through the residual layer.²⁷

Importantly, in the case of applying the hybrid ARS (Fig. 6, solid lines), the variation in J_{SC} produced by the changes in σ and d_R is much smaller than the case of applying the moth eye coating (Fig. 6, dashed lines). For example, the size of the variation in J_{SC} , shown in Fig. 6a (vertical two-headed arrows), is 0.4% and 2.2% (>5 times difference) for the cases of using the hybrid ARS and moth eye, respectively. Although the smooth refractive index profile produced by moth eye surface shows a remarkable AR performance,^{18,20} the existence of the residual layer as well as the clearance in the adjacent cones necessarily disrupts the smoothness of refractive index profile, decreasing the performance. The results given here suggest that the hybridization of the moth eye structure and IF layers, used in the proposed AR design, is quite useful to compensate for the effects of such disrupted refractive index profile and enhance the robustness of performance.

Photocurrent loss by the absorption in glass substrate

The optical data in Fig. 2a (dashed lines) suggests that, at a short wavelength range (<400 nm), the level of absorption in the high- n glass used in our experiment is much greater than that in the normal glass, which could decrease the efficiency of the proposed system. To quantify this effect, we evaluated the photocurrent loss due to the glass absorption ΔJ_{SC}^G , which is described as follows:

$$\Delta J_{SC}^G = \int_0^{\lambda_g} q_e \Delta N_p^G(\lambda) F_{NR}(\lambda) d\lambda, \quad (15)$$

$$\Delta N_p^G(\lambda) = A_0(\lambda) F(\lambda) \frac{\lambda}{hc}. \quad (16)$$

Here, $\Delta N_p^G(\lambda)$ is the number of photons, corresponding to the wavelength λ , which are lost due to the glass absorption, and $A_0(\lambda)$ is the absorbance in the glass substrate equation (8) at λ . In equations (15) and (16), the loss of photocurrent is calculated by summing the loss of photons over the wavelength range below the bandgap wavelength of P3HT (λ_g), similar to equations (13) and (14). As shown in Table 1, the level of ΔJ_{SC}^G for the high- n glass substrate is much greater than that for the normal- n glass substrate (+145.4 to +165.4%, depending on the AR configuration), although the two types of glass have the same thickness (0.7 mm). Table 1 also suggests that for the device with the hybrid ARS and high- n glass substrate (i.e., the proposed AR design), the ratio of $\Delta J_{SC}^G/J_{SC}$ is 3.25%. This value appears to be not negligible compared to the total AR effect of the proposed device (4.02%; Table 1), meaning that the glass absorption should be considered to be a factor that can actually degrade the AR performance. This result also indicates a future possibility that the performance of the proposed system could be further improved by the development of the high- n glass with a wide transparent wavelength region, which is being explored from various approaches.^{48–50}

Experimental testing

We experimentally measured the spectral dependence of photocurrent generation for the verification of optical simulation. The OPV cell was deposited on the high- n glass substrate ($n_D = 1.75$), and the change in EQE produced by the hybrid ARS or two-layer IF coating was compared with the corresponding simulation results. The SEM micrograph of the moth eye structure, fabricated by nanoimprint lithography, is presented in Fig. 7a.

As shown in Fig. 7b, the level of EQE was increased by applying the hybrid ARS or the IF layers over a wide range of wavelengths. By calculating the ratio of

EQE with and without ARS, we found that the increase rate of EQE by the hybrid ARS and IF layers was similar to that predicted from the numerical simulation (Fig. 7c). We converted the data of EQE to the level of J_{SC} under the light sources of sunlight, LED, and fluorescent lamp, and confirmed that the increase rate of J_{SC} by both types of ARS is similar for the experimental and simulation data (Fig. 7d). The data shown in Table 2 also suggest that the increase in J_{SC} by the hybrid ARS (6.10–6.29%) is significantly greater than that by the IF layers (4.66–4.69%). The numerical result in Table 1 shows that in the absence of ARS, J_{SC} obtained with the high- n glass substrate is 3.11% lower than that obtained with the normal glass substrate under sunlight illumination. Therefore, by considering together this numerical result and the experimentally measured performance enhancement by the hybrid ARS (6.29%; Table 2), we can predict that the performance of the OPV cell with the proposed AR design will be around 3.2% higher than that of the reference cell.

Although the experimental results serve to support the validity of our optical simulation, a drawback of the device used in the experiment is that it contains the normal- n glass substrate (see Experimental), which is not included in the model of the proposed device (Fig. 1c). The numerical analysis predicts that the light absorption in the normal- n glass substrate with 0.7 mm thickness corresponds to the photocurrent loss of around 1.27% (Table 1), which would cause the decrease in the measured performance of OPVs. In the future work, we are planning to construct the proposed OPV device without using the normal- n glass to further improve the performance.

Conclusion

We proposed an optical design for OPVs integrating the hybrid ARS, which consists of the moth eye and two-layer IF coating,¹² with the high- n glass substrate (Fig. 1c). Through the optical analysis using the characteristic matrix-based method,²⁷ we showed that the effectiveness of the high- n glass substrate significantly depends on the AR configuration. When the refractive index of the glass substrate increases, the level of J_{SC} monotonically decreases in the absence of ARS, monotonically increases in the presence of the hybrid ARS or IF coating, and has a local maximum in the presence of moth eye coating (Fig. 3). We revealed that the usefulness of the high- n glass substrate is determined by which is greater between the reflection at the front and back sides of the substrate, and the high- n glass becomes the most useful when the front-side reflection is nearly fully suppressed by the hybrid ARS (Fig. 9). We also demonstrated that the proposed AR design has many advantages such as an excellent wide-angle performance for both the indoor and outdoor light conditions (Fig. 4) and a high robustness

against the variations in geometric features of moth eye texture (Fig. 6). Additionally, we experimentally measured the change in EQE by the addition of the hybrid ARS and IF layers for the OPV cell deposited on the high- n glass substrate and confirmed that the increase rate of EQE is similar to the prediction by the optical simulation (Fig. 7). The proposed AR design concept is beneficial to extend our options available for broadband and omnidirectional antireflection for OPVs.

Acknowledgments This study was partially supported by KAKENHI (26390025) from the Japanese government, and JST CREST. We thank Toppan Printing for offering the nanoimprint mold used in the experiment.

Appendix 1: FDTD analysis for evaluating the dependence of J_{SC} on the moth eye period

In order to check the validity of the effective medium approximation used in this study, we examined the change in the photocurrent of OPVs associated with the change in the moth eye period by using FDTD simulation. In the FDTD model, the moth eye structure was attached to the front surface of the OPV device shown in Fig. 1a. The optical data of the materials were taken from the data used in our previous study,¹³ which is described by the Lorentz-Drude model³⁷ (different from the data used for the characteristic matrix-based analysis). The Lorentz-Drude formulation of optical data is required to enable efficient FDTD simulations for dispersive materials, because the FDTD algorithm generally results in a very high computational cost.⁴⁰ To estimate J_{SC} , we first obtained the absorbance in the active layer from the FDTD simulation. When the light passes through a glass substrate, the FDTD response shows strong oscillation due to the artificial interference effect.¹³ Therefore, the computational algorithm proposed by the previous study¹³ was applied to remove this effect and accurately estimate the absorbance spectrum ($A_p(\lambda)$ in equation (13)). Then, the value of J_{SC} was calculated under the AM1.5 spectrum by using equations (13) and (14).

As shown in Fig. 8a, the level of J_{SC} was plotted as a function of the moth eye period (L) for three cases of cone height ($H = 200$ (solid), 600 (dashed), or 1000 nm (dotted)). To describe more clearly the dependence of J_{SC} on the texture period, we calculated its relative change compared to the case with $L = 32$ nm for each H (Fig. 8b). The reference value of L (32 nm) was selected to be much smaller than the minimum wavelength of sunlight (300 nm) so that the effective medium approximation is reasonably valid at this L value. Figure 8b shows that the J_{SC} level increases approximately linearly as a function of L , when L is

smaller than 300 nm. The relative change in J_{SC} for the L range used in this study ($L < 300$ nm) is smaller than 0.2%, suggesting that the effective medium approximation can be considered quite valid for the current simulation.

Appendix 2: Dependence of the effectiveness of applying high- n glass substrate on AR configurations

In this appendix, we analyze the reason why the relationship between the refractive index of glass substrate and the performance of OPVs is qualitatively modified by the configuration of ARS (Fig. 3). We first attempt to decompose the reflection of incident light into the reflection at the front and back sides of the glass substrate. As illustrated in Fig. 9a, the overall reflectance R_t of the device can be expressed as the sum of the irradiance R_a of the light reflected at the front side of the substrate and the irradiance R_k^n of the light that has been reflected n times (for $n = 1, 2, \dots$) at the back side of the substrate and has returned to the incident medium. Therefore, we can find

$$R_t = R_a + \sum_{n=1}^{\infty} R_k^n, \quad (17)$$

where R_k^n can be obtained as $R_k^n = T_a T_b R_c (R_b R_c)^{n-1}$ from Fig. 1d.

Here, let us consider a case where the level of absorbance in the OPV cell is relatively high and the intensity of incident light is rapidly weakened through the repeated reflections within the glass substrate. In this case, it may be assumed that the level of overall reflectance is largely determined by considering only one reflection at each of the front and back sides of the substrate, similar to the assumption used for the vector method in optical theory.²⁷ With this assumption, the reflectance can be approximated such that $R_t \approx \tilde{R}_t$ with

$$\tilde{R}_t = R_a + R_k^1, \quad (18)$$

where the sum of R_k^n for $n \geq 2$ (Fig. 9a, dashed lines) has been neglected from equation (17). If this approximation holds, the reflectance can be decomposed into R_a and R_k^1 , which represent the intensities of the reflection at the front side and back side of the substrate, respectively (Fig. 9a).

We plotted the change in reflectance R_t as a function of the refractive index of the glass substrate (n_G), for the device with different AR configurations (Figs. 9b–9e, black dashed lines). Here, the wavelength was selected to be $\lambda = 500$ nm, at which the level of photocurrent becomes maximum (Figs. 5b and 7b). Thus, it can be expected that the performance of OPVs is strongly affected by the AR function at this wavelength. Figures 9b–9e (black solid lines) also show

the change in \tilde{R}_t , which indicates that the level of R_t can be approximated very well by that of \tilde{R}_t . In fact, the relative difference between them (i.e., $|\tilde{R}_t/R_t - 1| \times 100$) was found to be less than 0.07% for all the cases, meaning the validity of the approximation equation (18). This is because a large portion (> 88%; Fig. 5b) of incident light is absorbed in the active layer at the examined wavelength (500 nm) so that the light waves that have been reflected more than one time at the back side of the substrate are very weak.

To compare the components of reflectance produced by the reflection at the front and back sides of the substrate, we plotted the changes in R_a and R_k^1 in Figs. 9b–9e (blue and red lines). From the relationship between R_a and R_k^1 , we can largely understand how the AR configuration alters the effectiveness of the high- n glass substrate (Fig. 3), as follows. For the case without ARS (Fig. 9b), since strong reflection occurs at the front surface of the device, R_a is always greater than R_k^1 and therefore the change in reflectance is mainly determined by the change in R_a . Since R_a increases with increasing the difference in refractive index between the glass substrate and air, larger n_G results in stronger reflection (Fig. 9b, black lines), leading to the decrease in the performance of OPVs (Fig. 3a).

In contrast, for the case of applying the hybrid ARS or IF layers (Figs. 9c and 9d), R_a is maintained at a low level due to the antireflection effect so that R_a is smaller than R_k^1 . Therefore, the level of overall reflectance is mainly determined by the change in R_k^1 . Note that the back-side reflection is weakened by increasing n_G , because larger n_G reduces the mismatch in the optical admittance between the glass substrate and the thin-film assembly of the OPV cell,²⁷ which includes the materials with higher refractive index (Fig. 2c), as mentioned above. Thus, the use of the high- n glass substrate can decrease the level of overall reflectance (Figs. 9c and 9d, black lines) and thereby improve the solar cell performance (Fig. 3b).

Only when the moth eye coating is applied (Fig. 9e), the relation between R_a and R_k^1 is reversed with changing n_G such that $R_a < R_k^1$ and $R_a > R_k^1$ in the ranges of small and large values of n_G , respectively. With the moth eye coating, larger n_G increases the difference in refractive index between the moth eye and glass substrate, and significantly increases the level of R_a from almost zero (Fig. 9e, blue line). This is because the moth eye is assumed to be fabricated by polymer nanoimprinting and have a low refractive index of 1.5,²⁶ as mentioned above. On the other hand, larger n_G decreases the level of R_k^1 similar to the cases with the other types of ARS (Figs. 9b–9d), switching the magnitudes of R_a and R_k^1 . Due to this switching, the overall reflectance takes a local minimum at $n_G = \sim 1.75$ (Fig. 9e, black lines) and therefore the performance of OPVs takes a local maximum at around the same value of n_G (Fig. 3b, dashed lines). The argument in the appendix suggests that the effectiveness of the

high- n glass substrate strongly depends on which between the front- and back-side reflection is larger, and the use of the high- n glass is effective only when the front-side reflection is sufficiently smaller than the back-side reflection.

References

1. Yu, G, Gao, J, Hemmelen, JC, Wudl, F, Heeger, AJ, “Polymer Photovoltaic Cells: Enhanced Efficiencies via a Network of Internal Donor-Acceptor Heterojunctions.” *Science*, **270** 1789–1791 (1995)
2. Sariciftci, NS, Smilowitz, L, Heeger, AJ, Wudl, F, “Photoinduced electron Transfer from a Conducting Polymer to Buckminsterfullerene.” *Science*, **258** 1474–1476 (1992)
3. Park, SH, Roy, A, Beaupre, S, Cho, S, Coates, N, Moon, JS, Moses, D, Leclerc, M, Lee, K, Heeger, AJ, “Bulk Heterojunction Solar Cells with Internal Quantum Efficiency Approaching 100%.” *Nat. Photonics*, **3** 297–303 (2009)
4. Krebs, FC, Espinosa, N, Hösel, M, Sondergaard, RR, Jorgensen, M, “25th Anniversary Article: Rise to Power—OPV-Based Solar Parks.” *Adv. Mater.*, **26** 29–39 (2014)
5. Minnaert, B, Veelaert, P, “A Proposal for Typical Artificial Light Sources for the Characterization of Indoor Photovoltaic Applications.” *Energies*, **7** 1500–1516 (2014)
6. Minnaert, B, Veelaert, P, “The Appropriateness of Organic Solar Cells for Indoor Lighting Conditions.” *Proc. SPIE*, **7722** 77221P (2010)
7. Steim, R, Ameri, T, Schilinsky, P, Waldauf, C, Dennler, G, Scharber, M, Brabec, CJ, “Organic Photovoltaics for Low Light Applications.” *Sol. Energ. Mat. Sol. Cells*, **95** 3256–3261 (2011)
8. Bachmann, J, Buerhop-Lutz, C, Steim, R, Schilinsky, P, Hauch, JA, Zeira, E, Christoh, B, “Highly Sensitive Non-contact Shunt Detection of Organic Photovoltaic Modules.” *Sol. Energ. Mat. Sol. Cells*, **101** 176–179 (2012)
9. Scharber, MC, Sariciftci, NS, “Efficiency of Bulk-Heterojunction Organic Solar Cells.” *Prog. Polym. Sci.*, **38** 1929–1940 (2013)
10. Gollu, SR, Sharma, R, Srinivas, G, Kundu, S, Gupta, D, “Incorporation of SiO₂ Dielectric Nanoparticles for Performance Enhancement in P3HT:PCBM Inverted Organic Solar Cells.” *Organic Electronics*, **24** 43–50 (2015)
11. Kulkarni, AP, Noone, KM, Munechika, K, Guyer, SR, Ginger, DS, “Plasmon-Enhanced Charge Carrier Generation in Organic Photovoltaic Films Using Silver Nanoprisms.” *Nano Letters*, **10** 1501–1505 (2010)
12. Kubota, S, Kanomata, K, Suzuki, T, Ahmmad, B, Hirose, F, “Hybrid Antireflection Structure with Moth Eye and Multilayer Coating for Organic Photovoltaics.” *J. Coat. Technol. Res.*, **12** 37–47 (2015)
13. Kubota, S, Kanomata, K, Ahmmad, B, Mizuno, J, Hirose, F, “Optimized Design of Moth Eye Antireflection Structure for Organic Photovoltaics.” *J. Coat. Technol. Res.*, **13** 201–210 (2016)
14. Boden, SA, Bagnall, DM, “Optimization of Moth-Eye Antireflection Schemes for Silicon Solar Cells.” *Prog. Photovolt. Res. Appl.*, **18** 195–203 (2010)
15. Brunner, R, Sandfuchs, O, Pacholski, C, Morhard, C, Spatz, J, “Lessons from Nature: Biomimetic Subwavelength Structures for High-Performance Optics.” *Laser Photonics Rev.*, **6** 641–659 (2012)

16. Sun, CH, Jiang, P, Jiang, B, “Broadband Moth-Eye Antireflection Coatings on Silicon.” *Appl. Phys. Lett.*, **92** 061112 (2008)
17. Huang, YF, Chattopadhyay, S, “Nanostructure Surface Design for Broadband and Angle-Independent Antireflection.” *J. Nanophotonics*, **7** 073594 (2013)
18. Deinega, A, Valuev, I, Potapkin, B, Lozovik, Y, “Minimizing Light Reflection from Dielectric Textured Surfaces.” *J. Opt. Soc. Am. A*, **28** 770–777 (2011)
19. Forberich, K, Dennler, G, Scharber, MC, Hingerl, K, Fromherz, T, Brabec, CJ, “Performance Improvement of Organic Solar Cells with Moth Eye Anti-Reflection Coating.” *Thin Solid Films*, **516** 7167–7170 (2008)
20. Chen, M, Chang, HC, Chang, ASP, Lin, SY, Xi, JQ, Schubert, EF, “Design of Optical Path for Wide-Angle Gradient-Index Antireflection Coatings.” *Applied Optics*, **46** 6533–6538 (2007)
21. Han, KS, Shin, JH, Yoon, WY, Lee, H, “Enhanced Performance of Solar Cells with Anti-Reflection Layer Fabricated by Nano-imprint Lithography.” *Sol. Energ. Mat. Sol. Cells*, **95** 288–291 (2011)
22. John, J, Tang, YY, Rothstein, JP, Watkins, JJ, Carter, KR, “Large-Area, Continuous Roll-to-Roll Nanoimprinting with PFPE Composite Molds.” *Nanotechnology*, **24** 505307 (2013)
23. Boltasseva, A, “Plasmonic Components Fabrication via Nanoimprint.” *J. Opt. A*, **11** 114001 (2009)
24. Brigo, L, Mattei, G, Michieli, N, Brusatin, G, “2D Photonic Gratings from Thermal Imprinting of ITO-Based Films.” *Microelectron. Eng.*, **97** 193–196 (2012)
25. Kim, E, Cho, Y, Park, KT, Choi, JH, Lim, SH, Cho, YH, Nam, YH, Lee, JH, Kim, DW, “Mie Resonance-Mediated Antireflection Effects of Si Nanocone Arrays Fabricated on 8-in Wafers Using a Nanoimprint Technique.” *Nanoscale Research Letters*, **10** 164 (2015)
26. Lü, C, Yang, B, “High Refractive Index Organic-Inorganic Nanocomposites: Design, Synthesis and Application.” *J. Mater. Chem.*, **19** 2884–2901 (2009)
27. Macleod, HA, *Thin-Film Optical Filters*, 4th ed. CRC Press, Boca Raton (2010)
28. Otto, M, Bender, M, Richter, F, Hadam, B, Kliem, T, Jede, R, Spangenberg, B, Kurtz, H, “Reproducibility and Homogeneity in Step and Repeat UV-Nanoimprint Lithography.” *Microelectron. Eng.*, **73–74** 152–156 (2004)
29. Bouhafs, D, Moussi, A, Chikouche, A, Ruiz, JM, “Design and Simulation of Antireflection Coating Systems for Optoelectronic Devices: Application to Silicon Solar Cells.” *Sol. Energy Mater. Sol. Cells*, **52** 79–93 (1998)
30. ASTM G173-03, “Standard Tables for Reference Solar Spectral Irradiances, ASTM International.” West Conshohocken, Pennsylvania, 2005
31. Kubota, S, Kanomata, K, Momiyama, K, Suzuki, T, Hirose, F, “Robust Design Method of Multilayer Antireflection Coating for Organic Solar Cells.” *IEICE Trans. Electron.*, **E96-C** 604–611 (2013)
32. Raut, HK, Dinachali, SS, He, AY, Ganesh, VA, Saifullah, MSM, Law, J, Ramakrishna, S, “Robust and Durable Polyhedral Oligomeric Silsesquioxane-Based Anti-Reflective Nanostructures with Broadband Quasi-Omnidirectional Properties.” *Energy Env. Sci.*, **6** 1929–1937 (2013)
33. Tommila, J, Aho, A, Tukiainen, A, Polojärvi, V, Salmi, J, Niemi, T, Guina, M, “Moth-Eye Antireflection Coating Fabricated by Nanoimprint Lithography on 1 eV Dilute Nitride Solar Cell.” *Prog. Photovolt.: Res. Appl.*, **21** 1158–1162 (2013)
34. Yu, Z, Gao, H, Wu, W, Ge, H, Chou, SY, “Fabrication of Large Area Subwavelength Antireflection Structures on Si Using Trilayer Resist Nanoimprint Lithography and Liftoff.” *J. Vac. Sci. Technol. B*, **21** 2874–2877 (2003)
35. Lee, SH, Han, KS, Shin, JH, Hwang, SY, Lee, H, “Fabrication of Highly Transparent Self-Cleaning Protection Films for Photovoltaic Systems.” *Prog. Photovolt.: Res. Appl.*, **21** 1056–1062 (2013)
36. Otto, M, Bender, M, Hadam, B, Spangenberg, B, Kurtz, H, “Characterization and Application of a UV-Based Imprint Technique.” *Microelectron. Eng.*, **57–58** 361–366 (2001)
37. Rakic, AD, Djuricic, AB, Elazar, JM, Majewski, ML, “Optical Properties of Metallic Films for Vertical-Cavity Optoelectronic Devices.” *Appl. Opt.*, **37** 5271–5283 (1998)
38. Fujiwara, H, *Spectroscopic Ellipsometry: Principles and Applications*. John Wiley and Sons Ltd, West Sussex (2007)
39. Aspnes, DE, “Optical Properties of Thin Films.” *Thin Solid Films*, **89** 249–262 (1982)
40. Taflove, A, Hagness, SC, *Computational Electrodynamics: The Finite-Difference Time-Domain Method*. Artech House Inc., Norwood (2005)
41. Persson, NK, Inganas, O, “Organic Tandem Solar Cells – Modeling and Predictions.” *Sol. Energ. Mat. Sol. Cells*, **90** 3491–3507 (2006)
42. Persson, NK, Inganas, O, “Simulations of Optical Processes in Organic Photovoltaic Devices.” In: Sun, SS, Sariciftci, NS (eds.) *Organic Photovoltaics: Mechanisms, Materials, and Devices*, pp. 107–138. CRC Press, Boca Raton (2005)
43. Darkwi, AY, Lote, WK, Ibrahim, K, “Computer Simulation of Collection Efficiency of a-Si: H Tandem Solar Cells Interconnected by Transparent Conductive Oxide.” *Sol. Energ. Mater. Sol. Cells*, **60** 1–9 (2000)
44. Colorimetry, 3rd ed., CIE 15:2004, International Commission on Illumination, Vienna, Austria, 2004
45. Ren, W, Zhang, G, Wu, Y, Ding, H, Shen, Q, Zhang, K, Li, J, Pan, N, Wang, X, “Broadband Absorption Enhancement Achieved by Optical Layer Mediated Plasmonic Solar Cell.” *Optics Express*, **19** 26536–26550 (2011)
46. Li, X, Li, PC, Ji, L, Stender, C, McPheeters, C, Tatavarti, SR, Sablon, K, Yu, ET, “Subwavelength Nanostructures Integrated with Polymer-Packaged iii-v Solar Cells for Omnidirectional, Broad-Spectrum Improvement of Photovoltaic Performance.” *Prog. Photovolt. Res. Appl.*, **23** 1398–1405 (2015)
47. Minot, MJ, “The Angular Reflectance of Single-Layer Gradient Refractive-Index Films.” *J. Opt. Soc. Am.*, **67** 1046–1050 (1977)
48. Masuno, A, Inoue, H, “High Refractive Index of 0.30La₂O₃–0.70Nb₂O₅ Glass Prepared by Containerless Processing.” *Appl. Phys. Express*, **3** 102601 (2010)
49. Mao, Z, Duan, J, Zheng, X, Zhang, M, Zhang, L, Zhao, H, Yu, J, “Study on Optical Properties of La₂O₃–TiO₂–Nb₂O₅ Glasses Prepared by Containerless Processing.” *Ceram. Intern.*, **41** S51–S56 (2015)
50. Xiang, H, Guan, L, Peng, Z, Li, J, “Preparation of High Refractive Index La₂O₃–TiO₂ Glass by Aerodynamic Levitation Technique and Effects of Bi₂O₃ Substitution on its Thermal and Optical Properties.” *Ceram. Intern.*, **40** 4985–4988 (2014)